AGU PUBLICATIONS

Geochemistry, Geophysics, Geosystems

RESEARCH ARTICLE
10.1002/2016GC006610

Key Points:
- High heat flow is metamorphosing very young sediment in the Imperial Valley and highest heat flow creates shallowest metamorphism
- Metamorphism of sediment is creating new crystalline crust to >7 km depth in the Imperial Valley and most earthquakes are in this new crust
- Progressive metamorphism creates no discontinuities and the velocity gradient with depth decreases where rock porosity is reduced to 5–10%

Correspondence to:
L. Han,
lianghan@vt.edu

Citation:
Han, L., J. A. Hole, J. M. Stock, G. S. Fuis, C. F. Williams, J. R. Delph, K. K. Davenport, and A. J. Livers (2016), Seismic imaging of the metamorphism of young sediment into new crystalline crust in the actively rifting Imperial Valley, California, *Geochem. Geophys. Geosyst.*, *17*, 4566–4584, doi:10.1002/2016GC006610.

Received 29 AUG 2016
Accepted 28 OCT 2016
Accepted article online 3 NOV 2016
Published online 18 NOV 2016

Seismic imaging of the metamorphism of young sediment into new crystalline crust in the actively rifting Imperial Valley, California

Liang Han[1,2], John A. Hole[1], Joann M. Stock[3], Gary S. Fuis[4], Colin F. Williams[4], Jonathan R. Delph[1,5], Kathy K. Davenport[1,6], and Amanda J. Livers[1,7]

[1]Department of Geosciences, Virginia Tech, Blacksburg, Virginia, USA, [2]Now at Institute for Geophysics, University of Texas, Austin, Texas, USA, [3]Seismological Laboratory, California Institute of Technology, Pasadena, California, USA, [4]U.S. Geological Survey, Menlo Park, California, USA, [5]Now at Department of Earth Science, Rice University, Houston, Texas, USA, [6]Now at College of Earth, Ocean, and Atmospheric Sciences, Oregon State University, Eugene, Oregon, USA, [7]Now at University of North Dakota Energy and Environmental Research Center, Grand Forks, North Dakota, USA

Abstract Plate-boundary rifting between transform faults is opening the Imperial Valley of southern California and the rift is rapidly filling with sediment from the Colorado River. Three 65–90 km long seismic refraction profiles across and along the valley, acquired as part of the 2011 Salton Seismic Imaging Project, were analyzed to constrain upper crustal structure and the transition from sediment to underlying crystalline rock. Both first arrival travel-time tomography and frequency-domain full-waveform inversion were applied to provide P-wave velocity models down to ~7 km depth. The valley margins are fault-bounded, beyond which thinner sediment has been deposited on preexisting crystalline rocks. Within the central basin, seismic velocity increases continuously from ~1.8 km/s sediment at the surface to >6 km/s crystalline rock with no sharp discontinuity. Borehole data show young sediment is progressively metamorphosed into crystalline rock. The seismic velocity gradient with depth decreases approximately at the 4 km/s contour, which coincides with changes in the porosity and density gradient in borehole core samples. This change occurs at ~3 km depth in most of the valley, but at only ~1.5 km depth in the Salton Sea geothermal field. We interpret progressive metamorphism caused by high heat flow to be creating new crystalline crust throughout the valley at a rate comparable to the ≥2 km/Myr sedimentation rate. The newly formed crystalline crust extends to at least 7–8 km depth, and it is shallower and faster where heat flow is higher. Most of the active seismicity occurs within this new crust.

1. Introduction

Continental rifting results in high heat flow and an elevated geotherm as hot mantle rises beneath the rift. The later stages of rifting produce a topographic low into which rivers can flow, depositing sediment. A combination of high temperature and rapid sedimentation may metamorphose the deep basin sediment. Metamorphism of very young sediment has been observed in the Salton Trough of southern California [*Muffler and White*, 1969; *McDowell and Elders*, 1980; *Fuis et al*., 1984; *Cho et al*., 1988; *Shearer et al*., 1988]. Due to the geographic extent of high heat flow [*Lachenbruch et al*., 1985] and the large river delta, metamorphism may occur at a regional scale and create a significant volume of new felsic crystalline crust. The rate of crustal growth by sedimentation and metamorphism is comparable to those by magmatic accretion at subduction-related island arcs and slow seafloor spreading centers [*Dorsey*, 2010]. This new crust may host shallow seismicity in the active rift [*Hauksson et al*., 2012], and it may eventually form a large component of the future passive continental margin.

The Salton Trough is an active sediment-filled rift basin, at the northern end of the Gulf of California extensional province (Figure 1) [e.g., *Elders et al*., 1972; *Lonsdale*, 1989; *Stock and Hodges*, 1989; *Larsen and Reilinger*, 1991]. It is being formed by extension between the plate-bounding right-lateral San Andreas (SAF), Imperial (IF), and Cerro Prieto (CPF) transform faults (Figure 1). The northern Imperial Valley and southern Salton Sea (Figure 1) is the active part of the Salton Trough between the SAF and IF, and is characterized by high heat flow, volcanic and geothermal activity (Figure 2), and seismicity. It is almost entirely below sea

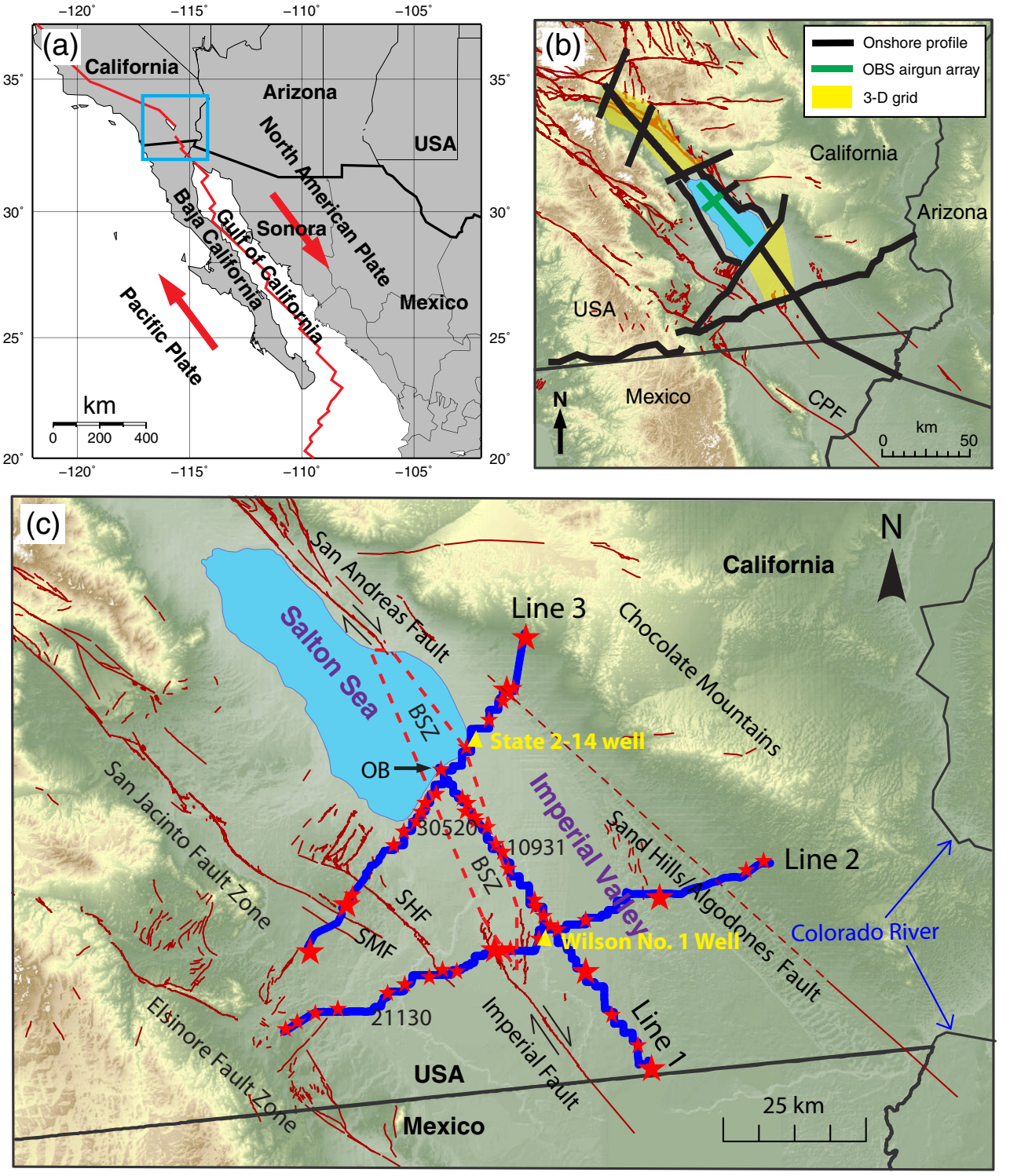

Figure 1. Salton Seismic Imaging Project (SSIP) study area and seismic lines used in this paper. (a) Rifts and transform faults of the plate boundary in California, Mexico, and the Gulf of California. Arrows show relative motion between Pacific plate and North America plate. Blue box is the survey area in Figure 1b. (b) Map of SSIP seismic lines. Thick black lines are onshore 2-D profiles, yellow-shaded areas are 3-D grids, and thick green lines in the Salton Sea are OBS arrays. Active faults are red. CPF, Cerro Prieto Fault. (c) Portions of SSIP Lines 1, 2, and 3 used in this study. Red stars are explosive shots, and larger stars correspond to shots >400 kg. Numbered shots are shown in data Figures 3–5. Blue dots are onshore seismographs. SHF, Superstition Hills Fault; SMF, Superstition Mountain Fault; BSZ, Brawley Seismic Zone; OB, Obsidian Butte. Interpreted Sand Hills/Algodones Fault is shown by dashed red line. Faults are from *Jennings and Bryant* [2010].

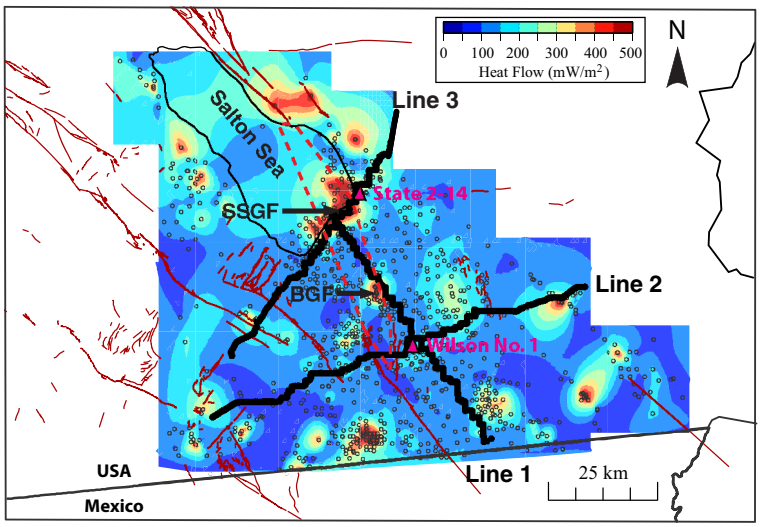

Figure 2. Heat flow in the Imperial Valley, compiled from *Newmark et al.* [1988], *Sass et al.* [1988], and the original data that were presented as gridded averages by *Lachenbruch et al.* [1985]. Small circles are well locations. Heat flow greater than 500 mW/m^2 was set as 500 mW/m^2. Data from wells were gridded in Matlab at 0.01 by 0.01 degree. Seismic lines and labels are the same as those in Figure 1. BGF, Brawley geothermal field; SSGF, Salton Sea geothermal field.

level; the elevation of the Salton Sea is −70 m. The Colorado River (Figure 1) has flowed into this active rift basin throughout the basin's history, carrying a high sediment load.

Heat flow in most of the Salton Trough is between 100 and 200 mW/m^2 (Figure 2) [*Lachenbruch et al.*, 1985], much larger than the mean global heat flow of 80 mW/m^2. In the Salton Sea Geothermal Field (Figure 2) in the northern Imperial Valley, heat flow exceeds 600 mW/m^2 in an arcuate zone ∼4 km wide and ∼12 km long [e.g., *Helgeson*, 1968; *Newmark* et al., 1988], roughly parallel to the five small Late Quaternary volcanic domes, the Salton Buttes, at the southern shore of the Salton Sea [e.g., *Robinson et al.*, 1976; *Schmitt and Vazquez*, 2006]. Significant seismicity occurs at 3–11 km depth in the oblique Brawley Seismic Zone (BSZ) (Figure 1) [*Hauksson et al.*, 2012] which connects the SAF and IF.

In the Salton Trough, most of the sediment and sedimentary rock was originally transported by the Colorado River from the Colorado Plateau [*Muffler and Doe*, 1968; *Herzig et al.*, 1988; *Dorsey*, 2010; *Dorsey and Lazear*, 2013]. The lithology from boreholes is dominantly lacustrine shale and siltstone, with minor amounts of sandstone and anhydrite, and mineralogy is consistent throughout the basin. Coarser alluvium derived from adjacent ranges is interbedded at the edges of the valley. Mineralogy changes systematically with depth, interpreted to be related to increasing temperature and progressive metamorphism of the sediment, not to changes in the source of the sediment [*Muffler and White*, 1969; *McDowell and Elders*, 1980; *Cho et al.*, 1988; *Shearer et al.*, 1988]. Greenschist facies metamorphism of the sediment is observed in wells throughout the valley starting at 0.6–2 km depth, and amphibolite grade is observed at ∼3 km depth within the Salton Sea geothermal field [*Muffler and White*, 1969; *Cho et al.*, 1988]. *Larsen and Reilinger* [1991] suggested a recent regional subsidence rate of 3 km/Myr from leveling data in the northern Imperial Valley. *Schmitt and Hulen* [2008] argued that the sedimentation rate accelerates toward the center of the Salton Trough, increasing from 2.2 to 3.8 km/Myr.

Numerous regional three-dimensional seismic velocity models have been built to study earthquake hazards in Southern California [e.g., *Magistrale et al.*, 1992; *Magistrale et al.*, 2000; *Lin et al.*, 2007; *Hauksson et al.*, 2012], but earthquake network data do not well constrain shallow structure in the valleys. Structure of the Imperial Valley in the upper crust was best studied by *Fuis et al.* [1984], who interpreted data from five seismic refraction profiles. One unreversed shot or two reversed shots were recorded on each profile on stations every 0.5–1 km. Low seismic velocity (2–5 km/s) was observed in the upper ∼4 km throughout the valley, underlain by crystalline rock that has slower seismic velocity than the valley margins. They interpreted the shallowest crystalline rock as metamorphosed sediment, based on low seismic velocity and the lack of a seismic reflection or velocity discontinuity associated with sediment deposited on crystalline rock.

The Salton Seismic Imaging Project (SSIP) acquired new controlled-source seismic data in the Salton Trough in 2011 [*Rose et al*., 2013]. *Persaud et al*. [2016] use some of these data to investigate basin structure and faulting in the Imperial Valley. This paper uses seismic imaging from a portion of the SSIP data set to study the transition from sediment to crystalline rock in the Imperial Valley, testing and improving models produced by the sparser data of *Fuis et al*. [1984]. The model of sedimentary metamorphism is tested by searching for a sediment-basement depositional discontinuity that might have remained undetected by the sparser seismic data and by correlating the higher-resolution seismic results with borehole and heat-flow observations. The new seismic velocity models confirm metamorphism and provide additional constraints on its depth and lateral extent.

2. Seismic Data

2.1. Data Acquisition

Seven refraction/wide-angle reflection profiles and two 3-D seismometer grids were acquired along and across the Salton Trough by SSIP in 2011 (Figure 1b) [*Rose et al*., 2013]. Both in-line and offline shots were recorded to provide three-dimensional data coverage. The recording systems were mostly single-component "Texan" (Ref Tek 125a) seismographs with geophones with a corner frequency of 4.5 Hz. Three-component 4.5 Hz geophones and RT130 (Ref Tek 130) seismographs were deployed every ∼1 km along Line 2. In total, 2781 land seismometers, with spacing as dense as 100 m, were deployed at over 4200 sites. A total of 126 buried explosive shots of 3–1400 kg were detonated. Thirty-eight ocean-bottom seismographs and 2330 small airgun shots were used in the Salton Sea.

In the Imperial Valley, three seismic lines were recorded, two of which went through the volcanic and geothermal field. In order to study the transition from sediment to basement in this basin, only the valley and near-valley portions of those three seismic profiles are used in this study (Figure 1c). Line 1 is parallel to the transform faults and relative plate motion direction (Figure 1). Twenty shot gathers were analyzed along the ∼65 km long portion of Line 1 in the Valley. Most shots were 115 kg, but a few were up to 1367 kg. The shots were recorded by 574 seismographs in the valley at a spacing of ∼100 m. There were 18 shots and 776 seismographs along the ∼90 km long valley portion of Line 2, oriented approximately perpendicular to the Imperial Fault (Figure 1). The receiver interval was ∼100 m in the west and middle of this line segment, but ∼200 m in the eastern third. The shot size was 115 kg, except the shot at the Imperial Fault was 911 kg and the shot to the east of the valley was 592 kg. The ∼67 km long portion of Line 3 consisted of 16 shots and 429 seismographs. This line crossed the valley perpendicular to the transform faults and along the Salton Sea geothermal field (Figure 2). On each side of the valley, two shots of >400 kg were fired, while in the valley, the shot size was either 115 or 229 kg. The receiver interval was ∼500 m in the western third of Line 3, ∼100 m in the valley, and ∼300 m to the east of the valley. Although larger shots were fired to the west of the valley, the signal recorded from these shots by the receivers inside the valley was poor. This was also observed during the seismic survey of *Fuis et al*. [1984] and is probably caused by basin margin structure to the west.

2.2. Data Description

Figure 3a illustrates the seismic phases that were observed throughout most of the valley. The inverse of the slope of the seismic arrivals indicates the apparent seismic velocity, which gradually increases from slow <2 km/s sediment near the surface (phase A) to turning (continuously refracted) waves with velocities >5 km/s representative of crystalline rock (phase B). The boundary between A and B is gradational and does not exhibit a sharp change in apparent velocity. No seismic reflection from the base of sediment is observed in data filtered at any frequency. The smooth increase in velocity, low crystalline-rock velocity, and lack of basement reflector are consistent with the observations of *Fuis et al*. [1984] that were interpreted as metamorphism of sediment, but the SSIP observations are much more densely constrained. Strong, multiple basin reverberations (phases C) are observed, indicative of a strong increase in velocity with depth, similar to the previous studies [*McMechan and Mooney*, 1980; *Fuis et al*., 1984]. Deeper crustal phases, such as the Moho reflection PmP and Moho refraction Pn, are observed in the valley at distances greater than 40 and 80 km, respectively [*Han et al*., 2016], but are not shown in this paper.

Arrivals very similar to those of Figure 3 are observed on all shots and stations within the central Imperial Valley (Figures 3–5), indicating only weak lateral variation in geologic structure throughout most of the

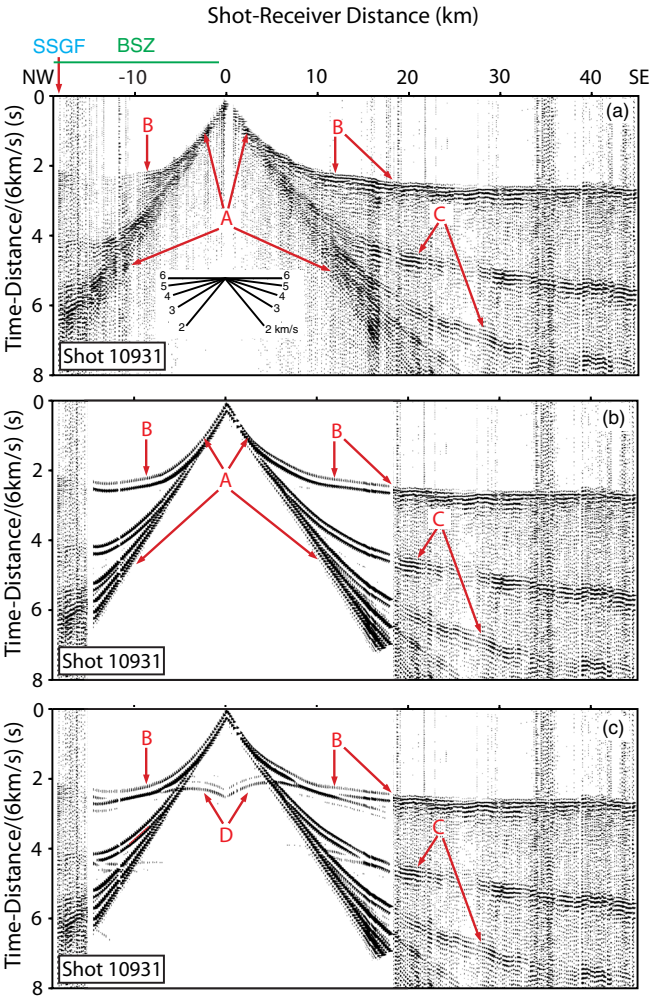

Figure 3. (a) Shot 10931 recorded along Line 1; see Figure 1 for location. Only the portion of the line in the Imperial Valley is shown. Travel time is reduced by 6 km/s. The data are bandpass filtered by an Ormsby filter at 5–8–20–30 Hz. Amplitudes are normalized for each station. Smaller signal at the northwest end of the figure is due to amplitude normalization of geothermal energy industrial noise. (b) Synthetic seismic data at 0.1–10 Hz computed within the northern portion of the seismic velocity model of Figure 7. (c) Synthetic seismic data at 0.1–10 Hz computed within the seismic velocity model of Figure 11a. Seismic phases A, direct or turning wave in sediment; B, turning waves in the crystalline crust in the valley; C, multiple of B in the sedimentary basin; D, reflection from the artificial velocity discontinuity in Figure 11a; this phase does not exist in the real data. BSZ, Brawley Seismic Zone; SSGF, Salton Sea geothermal field.

valley. An important exception is within the Salton Sea geothermal field at the southern shore of the Salton Sea, where phase B arrives ~0.5 s earlier than the rest of the central valley (Figures 3 and 5). Earlier arrival times for phase B indicate shallower crystalline rock beneath the Salton Sea geothermal field, but the transition from phase A to B is gradational, similar to the rest of the valley.

The data along Lines 2 and 3 have larger variation where they extend beyond the edges of the Imperial Valley (Figures 4 and 5). To the west of shot 21130 (Figure 4), the crystalline-rock phase E arrives much earlier than phase B, the velocity increase from A to E is much sharper, the apparent velocity of E is faster, and the basin reverberation is much weaker or absent. This shot and other shots to the west on line 2 indicate a much shallower basin, a sharper sediment-rock boundary, and a faster crystalline-rock velocity. The two western-most shots on line 3 that are included in the analysis (Figure 1c) and the two eastern-most shots on both Lines 2 and 3 display similar features. These observations map the edges of the main basin [*Persaud et al.*, 2016].

The crustal reflection phase observed in the data, phase G in Figure 4, is only observed on Line 2 at offset >20–22 km and only for shot-receiver midpoints west of the Imperial Fault. A similar phase was observed nearby by *Fuis et al.* [1984]. Phases A and B exhibit only very small changes across the Imperial Fault (e.g., Figure 4), indicating that basin and shallowest crystalline rock structure are similar. These minor differences and the existence of reflector G west of the fault represent two different rift segments. Based on travel time and offset, reflector G is at 12–13 km depth. Two-dimensional modeling of this reflector is beyond the scope of this paper, which focuses primarily on the Imperial Valley rift segment.

3. Travel-Time Tomography

3.1. Method

First arrivals were picked manually on all the shot gathers (e.g., Figure 6a). The estimated accuracy of those picks is less than a half period of the dominant signals, which is 40–50 ms within the offset range used in this study. This represents an upper limit and many picks have <25 ms accuracy.

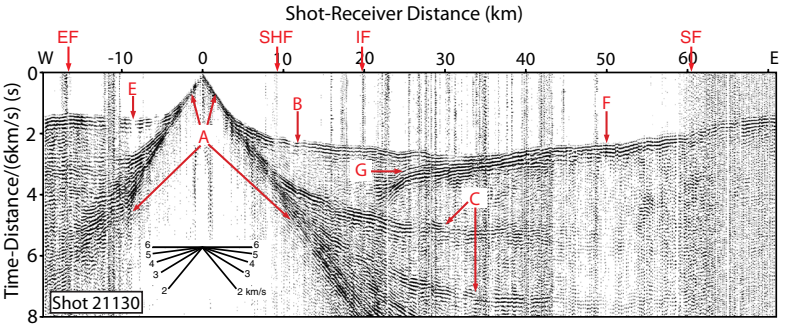

Figure 4. Shot 21130 recorded along Line 2, plotted and labeled similar to Figure 3. This line segment crosses the Imperial Fault (IF) and extends beyond farmland (lacustrine clay soil) onto the alluvial flanks of the Imperial Valley (Figure 1). Phase E, turning waves in the crystalline crust outside of the valley; phase F, same as B but with faster apparent velocity caused by the basin thinning eastward; phase G, reflection from the middle crust with midpoints west of the IF. EF, Elsinore Fault; SHF, Superstition Hills Fault; SF, Sand Hills Fault.

These first arrivals were inverted using the travel time tomography algorithm of *Hole* [1992]. Travel times and rays are computed using finite differences within a 3-D seismic velocity model [*Hole and Zelt*, 1995]. Rays are traced in 3-D to include the crooked line geometry, but the velocity is smoothed perpendicular to the line to create a 2-D model. The inversion uses smoothed back-projection. Weighting is used to eliminate the effects of uneven seismograph spacing. A moving average filter is applied to smooth the velocity perturbation before it is added to the previous velocity model. Rays and times are computed in the new model, and the inversion iterates to find the final model. The smoothing size is reduced gradually so that the initial iterations model large-scale structure, which is then used as the starting model for later iterations. This strongly reduces the effects of smooth starting models and pushes misfits toward smooth structure. The ratio between the horizontal and vertical smoothing is kept constant. Iterations are stopped before ray streaking artifacts are produced by model errors. The model resolution, i.e., the final smoothing size, is primarily limited by the shot spacing.

The starting velocity model for 2-D tomography was built using the same tomography process, but the horizontal smoothing was set large enough to keep the model 1-D, and the vertical smoothing was gradually decreased to 1 km. This simple 1-D model produces travel times that approximate the average observed times from all of the shots (e.g., Figure 6). For Lines 2 and 3, the 1-D starting model was derived using data only from the central basin, which is the focus of this paper. Strong velocity contrasts at shallow depth on the valley margins are not well represented by the smooth starting model and are less well constrained by sparser shots, so the tomography results are smoothed representations of actual structure outside the basins. A range of 1-D starting models with faster and slower velocity and with larger and smaller velocity gradients were tested. Within a reasonable range, smooth starting velocity models all produced similar final velocity structure, with larger variation outside the basin.

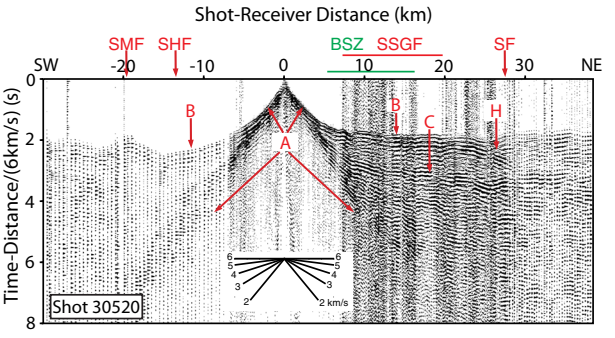

Figure 5. Shot 30520 recorded along Line 3, plotted and labeled the same as Figure 3. This line extends along the Salton Sea geothermal field (SSGF) near the volcanic domes, and extends beyond farmland onto the alluvial flanks of the Imperial Valley (Figure 1). The geothermal field is visible in the shot gathers as a region with higher industrial noise (7–20 km). Phase B to the east of the shot is ~0.5 s earlier within the SSGF than in most of the valley. First arrivals are earlier in the Superstition Mountains at distance −20 km, where granitic bedrock is exposed. Phase H, diffraction at the eastern edge of the deep basin. SMF, Superstition Mountain Fault.

The grid size used in this study is 100 m. A range of smoothing ratios were tested, and 5:1 allowed the best spatial resolution in a smooth model. The final tomography horizontal smoothing of Lines 1 and 3 was 2.5 km, which is roughly the average shot interval, and the vertical smoothing is 0.5 km. Line 2 was smoothed to 3.6 by 0.7 km due to the sparser average shot

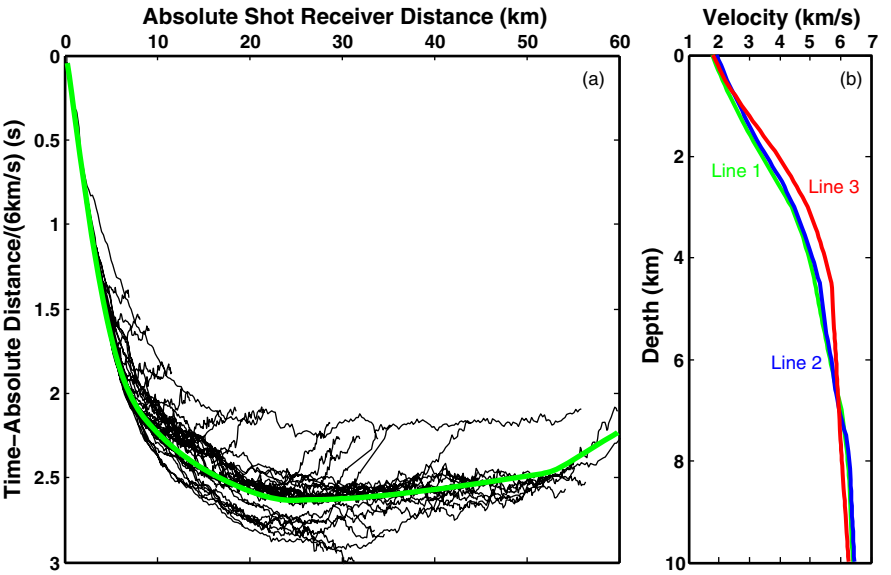

Figure 6. (a) Reduced first-arrival travel times for shots recorded along Line 1 (black lines) and synthetic times in green from the Line 1 model in Figure 6b. The earlier times correspond to the shot and stations in the Salton Sea geothermal field. Later times correspond to shots and receivers in southern Imperial Valley. (b) 1-D starting velocity models for Line 1, 2, and 3 derived from the first arrival travel times. The starting models for Lines 2 and 3 were derived using only shots and stations within the valley, and the velocity models are similar.

spacing. A smaller smoothing size results in more structural detail and a smaller data misfit, but produces artifacts parallel to the dominant ray directions that are caused by noise or picking uncertainty.

The ray coverage is very dense and crosses at multiple angles in the center of the models (Figures 7–9), providing strong constraints. At the bottom and edges of the models, ray coverage is sparser and mostly parallel to the boundaries, allowing for smearing of structure along these directions. The root-mean-square

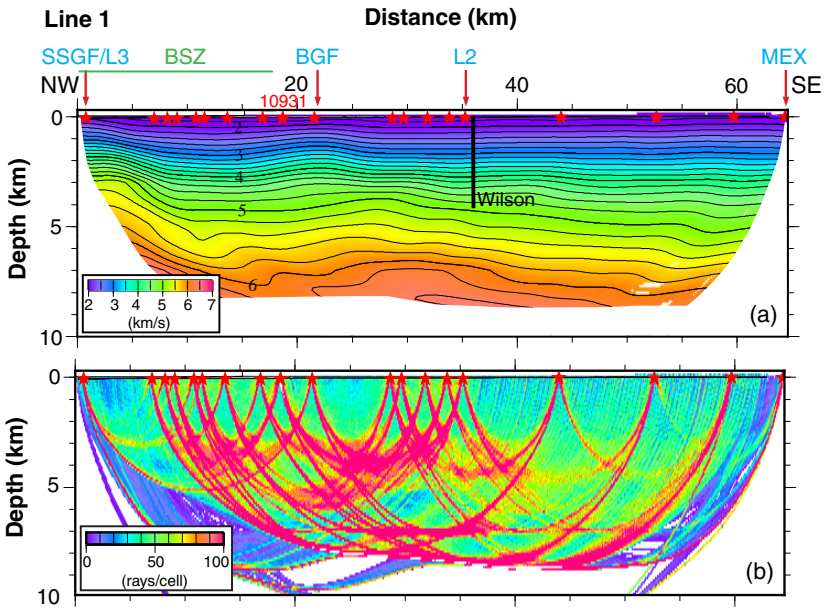

Figure 7. Line 1 upper crustal velocity model and ray coverage, at a vertical exaggeration of 2. Velocity is in km/s, and contours are at 0.2 km/s intervals. Ray coverage is plotted as hit count in 100 m grid cells. Regions without ray coverage are white. Red stars are shots and shot 10931 of Figure 3 is labeled. Vertical black line is the Wilson No. 1 well. SSGF, Salton Sea geothermal field; L2 and L3, intersections with Lines 2 and 3; BSZ, Brawley Seismic Zone; BGF, Brawley geothermal field; MEX, USA-Mexico border.

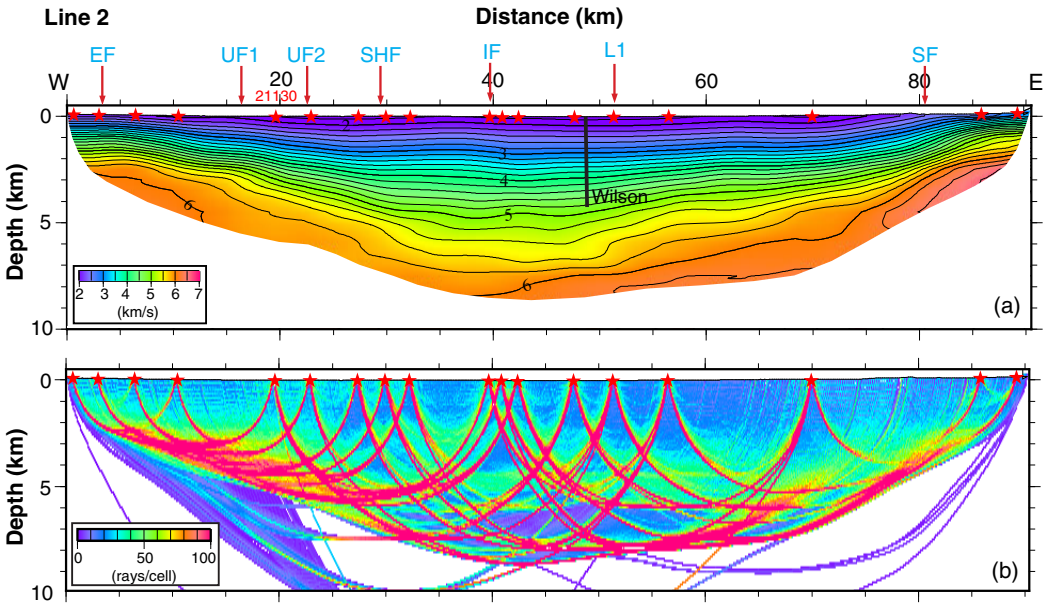

Figure 8. Line 2 upper crust velocity model and ray coverage, plotted as for Figure 7. Vertical black line is the Wilson No. 1 well. EF, Elsinore Fault Zone; UF1, unidentified fault at the west margin of the basin; UF2, unnamed fault characterized by a seismicity lineament connecting to the Superstition Mountain Fault [*Hauksson et al.*, 2012]; SHF, Superstition Hills Fault; IF, Imperial Fault; SF, interpreted location of Sand Hills Fault; L1, Line 1.

(RMS) data misfit for lines 1, 2, and 3, respectively is 36, 45, and 39 ms, within the picking accuracy (Figure 10).

3.2. Velocity Models

For Line 1, which is oriented northwest-southeast parallel to the relative plate motion direction, the velocity structure is almost 1-D (Figure 7). Velocity gradually increases from ~1.8 km/s at the surface to ~6 km/s at ~7 km depth approaching the maximum depth of good ray coverage. Velocity <3 km/s near the surface is typical for unconsolidated water-saturated clastic sediment [*Eberhart-Phillips et al.*, 1989]. The 4 km/s contour, typical of a well-lithified low-porosity shale or sandstone [*Han et al.*, 1986; *Eberhart-Phillips et al.*, 1989; *Johnston and Christensen*, 1995; *Vernik and Liu*, 1997], is nearly flat at ~3 km depth along the Imperial Valley. The velocity gradient with depth below 3–4 km depth is much smaller than that near the surface (Figures 7 and 15). There is no evidence of a steepening in the gradient that might indicate a smoothed discontinuity. Velocity >5 km/s, a rough proxy for crystalline metamorphic or igneous rock with very low porosity [e.g.,

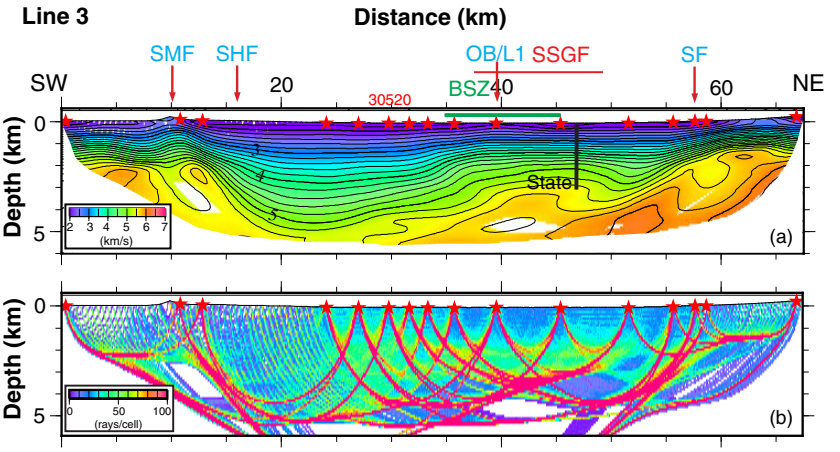

Figure 9. Line 3 upper crust velocity model and ray coverage, plotted as for Figure 7. Vertical black line is the State 2–14 well. OB, Obsidian Butte.

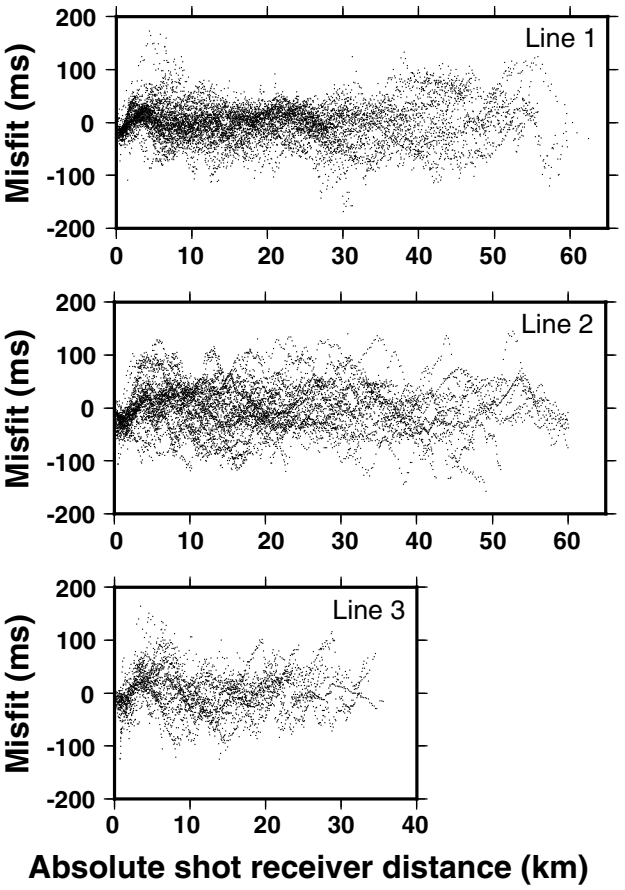

Figure 10. Travel time misfits (calculated minus observed) for the seismic velocity models of Figures 7–9. The RMS data misfit is 36, 45, and 39 ms for lines 1, 2, and 3, respectively.

Eberhart-Phillips et al., 1989; *Christensen and Mooney*, 1995], is at ~4.5 km depth in the northern Imperial Valley, and gradually deepens from the southern end of the Brawley seismic zone to ~5.5 km depth at the south end of the line. Fracturing in the seismic zone might be expected to reduce velocity, yet slightly higher crystalline-rock velocity is observed at a given depth in the seismic zone. High velocity is deeper toward the south, corresponding to both proximity to the mouth of the Colorado River and to slightly lower heat flow. Velocities of <4.5 km/s are slightly shallower near the Brawley geothermal field at model km ~21 on Line 1 (Figure 7). The SSGF, where higher velocity occurs at much shallower depth, is the only exception to nearly 1-D structure. This structure near the northwest edge of the model is not well constrained on Line 1, but is well resolved by Line 3. Deeper contours are uplifted a little to the south.

The west-east Line 2 crosses the center of the Imperial Valley and the northern end of the Imperial Fault, approximately perpendicular to Line 1. The deep sedimentary basin is ~60 km wide along this profile, with the deepest part near the Imperial Fault (Figure 8). Similar to Line 1, seismic velocity continuously increases in the deep basin, with a similar change in velocity gradient. There is a subtle deflection of the contour lines across the Imperial Fault, which may be smaller than can be resolved. Resolution of the margins of the deep basin are affected by the shot spacing and the tomography smoothing, such that lateral resolution is 3–4 km. Velocity contours rise slowly toward the eastern side of the basin, then rise sharply, consistent with a steep fault at model km ~80. This basin margin is east of the southeastern extrapolation of the San Andreas Fault but consistent with the inactive Sand Hills Fault, which is the along-strike extension of the Algodones Fault. In the western valley, the contours are consistent with the Superstition Hills Fault at model km ~30, and the basin margin at km ~17 may represent an unidentified fault. A seismicity lineament connecting to the Superstition Mountain Fault is observed at km ~22 [*Hauksson et al.*, 2012]. These structures define a complex western margin of the rift segment west of the transform Imperial Fault, and a complex step-over zone from the active Cerro Prieto and Imperial Faults to the San Jacinto Fault [*Magistrale*, 2002; *Persaud et al.*, 2016].

Line 3 extends southwest-northeast along the southern shore of the Salton Sea and along the axis of the geothermal field. The basin is about 45 km wide along this profile, with the deepest part near the western margin (Figure 9). Compared to Line 2, the basin is much narrower at this location, which limits the maximum recording offset and the imaging depth of the basin. Within the basin, the velocity model is only well constrained to ~5 km depth and <5.6 km/s. The basin boundaries are consistent with steep faults, with the western margin at or west of the Superstition Hills Fault, and the eastern margin consistent with the Sand Hills Fault. Phase H in Figure 5 is caused by energy diffracted off the edge of the shallow crystalline rock at the Sand Hills Fault. Similar to the other lines, velocity within the main basin increases continuously with depth, with a change in gradient. However, the velocity gradients are much larger within the Salton Sea geothermal field, and higher velocity occurs at much shallower depth (Figure 9). Shallow high velocity is

also observed within the Salton Sea geothermal field along Line 1 (Figure 7), but it is better constrained along this profile.

Travel-time tomography with smoothing successfully matches the data (Figure 10), but produces a model that is as smooth as possible. A sharp velocity discontinuity will be imaged as a zone with elevated velocity gradient. There is no evidence within the velocity models for a downward increase in the velocity gradient at any depth (Figures 7–9). In addition, no strong reflectors are observed in the data (Figures 3–5). These observations suggest that no velocity discontinuity, such as a depositional surface between sediment and bedrock, exists. However, smooth tomography is not the ideal tool to detect discontinuities, so synthetic seismograms and full-waveform inversion were used to further test for the presence or absence of a discontinuity.

4. Synthetic Seismograms

Full-waveform synthetic seismograms were computed for a representative shot in the central Imperial Valley. The algorithm of *Pratt* [1999] computes synthetic seismograms in a gridded 2-D velocity model using a finite-difference approximation of the acoustic wave equation in the frequency domain. Synthetic data were computed at 0.1–10 Hz for shot 10931 in the northern half of the travel-time tomography model of Figure 7. The synthetic data successfully reproduce the first arrivals and the strong basin reverberations (Figure 3b). The reverberations were not considered in the tomography, so their production in the synthetic data provides additional confidence in the velocity model, in particular the strong velocity gradient in the basin.

For comparison purposes, synthetic seismograms were computed for a similar velocity model, but containing a velocity discontinuity to simulate a depositional unconformity above basement (Figure 11a). This model was created by adding a velocity discontinuity from 4 to 5 km/s to the travel-time tomography model of Figure 7. The boundary is evident in the synthetic seismic data as a secondary reflection arrival, first arrival amplitude weakening at critical distance, and a slightly sharper change in the slope of first arrival (distance 10 km) and basin reverberation (distance 15 km at ~4 s) (Figure 3c), none of which are detected in the real data (Figure 3a). The lack of such evidence in the real data indicates that a strong discontinuity is not present under the Imperial Valley.

5. Full-Waveform Inversion

To improve the vertical resolution of the velocity model and to further test for the existence of discontinuities, full-waveform inversion was applied to the northern half of Line 1, where the shots are closest together.

5.1. Inversion Method

The full-waveform tomography algorithm of *Pratt* [1999] inverts phase and amplitude of seismic data in the frequency domain. An excellent starting model, accurate to within a half-period of the frequencies being inverted, is required for convergence. *Brenders and Pratt* [2007a, 2007b] demonstrate that a starting velocity model derived from first-arrival travel-time tomography works well for long-offset refraction and reflection data. An approach that progressively inverts from low to high-frequency stabilizes the inversion by producing more detailed starting models for inversions at higher frequency.

Land crustal seismic refraction and wide-angle reflection data are usually acquired along crooked roads, which makes 2-D full waveform inversion difficult. Due to the crooked SSIP line (Figure 1), an approximate 2-D geometry was used following *Smithyman and Clowes* [2012]. Similar to the travel-time tomography, the velocity and attenuation models are assumed to be homogeneous in the direction perpendicular to the average seismic line. Shots and receivers are projected to the straight line, and the seismic waveforms are corrected using a time shift determined by 3-D ray tracing, which accounts for the cross-line offsets produced by the crooked-line acquisition.

Densely spaced shots and receivers are required for full-waveform inversion to converge. At least one of the two domains must not be spatially aliased. The minimum velocity in the Imperial Valley is ~1.6 km/s, and the receiver interval is ~100 m, so ~8 Hz is the highest frequency that is not spatial aliased. The lowest

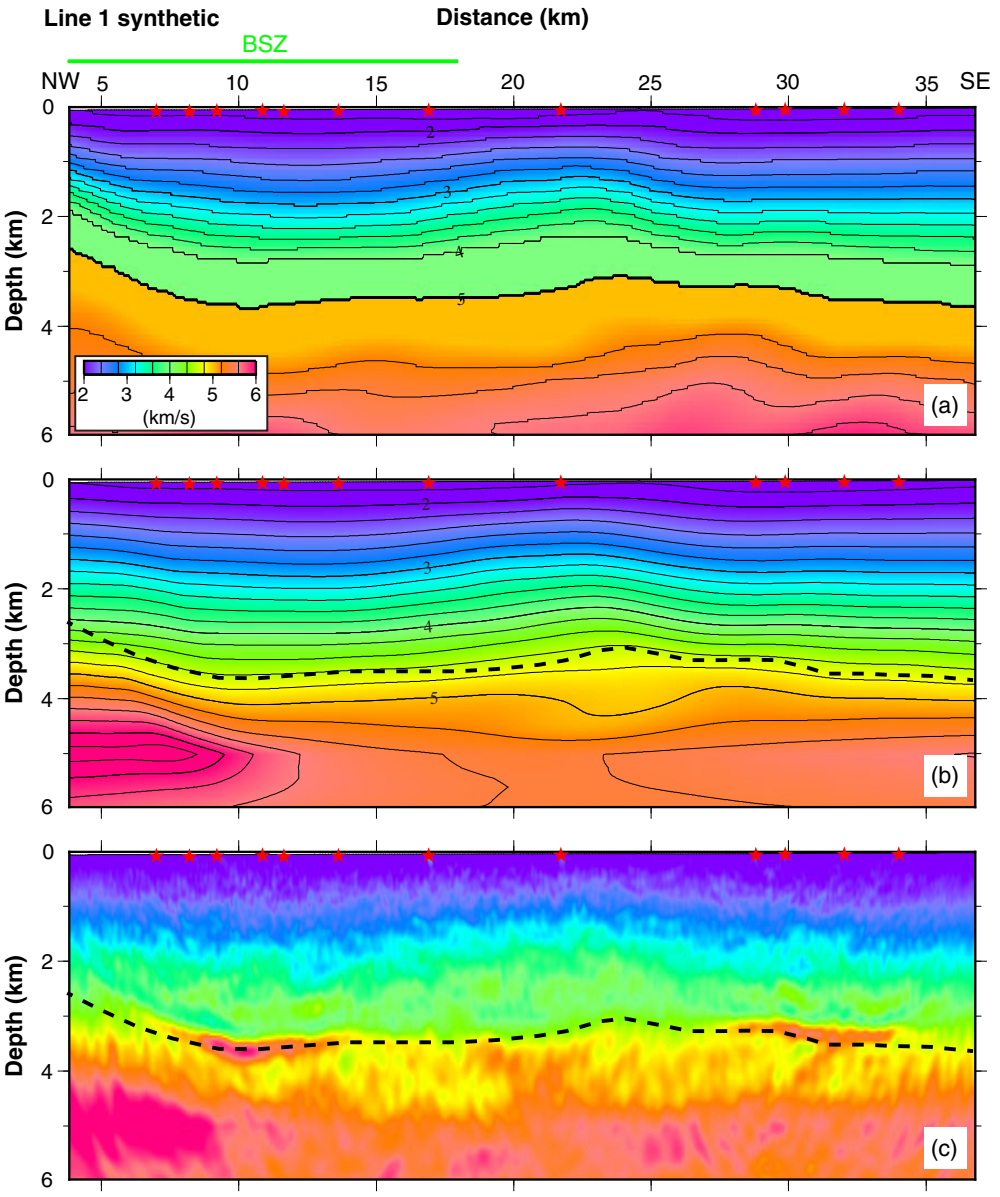

Figure 11. (a) Synthetic velocity model for a segment of Line 1, derived from the model of Figure 7 with an added 4 to 5 km/s discontinuity. This discontinuity is marked as black-dashed lines in Figures 11b and 11c. The x axis is labeled as for Figure 7. (b) Results of first arrival travel time tomography of synthetic seismic data for the shots shown as stars. (c) Results of full-waveform inversion of 2–7 Hz synthetic data. The discontinuity is detected as a sharp jump in velocity at the correct location.

frequency observed in the SSIP data is 2 Hz, so the data were inverted from 2 to 7 Hz. *Brenders and Pratt* [2007b] showed that full-waveform inversion can work if the shots are spatially aliased, but only up to a limit. The northern 30 km of Line 1 along the northern Imperial Valley has the densest shot spacing. Unfortunately, two shots could not be used because they were recorded only by every second station, which is not allowed by the existing software. The remaining shots are spaced ∼2.5 km on average, and ∼7 km at most. *Brenders and Pratt* [2007b] showed that the image quality remains acceptable if the shot spacing is less than 1.5 times the shortest wavelength recorded at the starting frequency, and accurate images can be obtained in the central portion of the model when the ratio is around 3.5, but the images suffer from some degradation. For the SSIP data, the ratio is ∼3 (0.8 km wavelength at 2 Hz at 1.6 km/s), so the shot spacing is nonideal. Additional challenges are the irregular shot spacing and noise in the data. *Bleibinhaus et al.* [2009] showed that the inversion of only the phase of the frequency-domain data is more stable for realistic long-offset data, so the SSIP inversion ignored amplitude. The inversion is thus similar to the finite-

Table 1. Full-Waveform Inversion Parameters[a]

Frequency (Hz)	No. of Iterations	Synthetic-Data Objective Function Reduction	Real-Data Objective Function Reduction
2	8	44%	22%
2.4	8	46%	22%
2.9	8	43%	24%
3.5	8	45%	34%
4.2	8	44%	46%
5	8	44%	43%
6	8	42%	52%
7	8	44%	48%

[a]The objective function defined by *Pratt* [1999] represents misfit.

frequency inversion method, but it uses the phase of a long-time window that can contain multiple arrivals rather than the travel time of a narrowly windowed single arrival. Data preprocessing included removal of noisy data traces and bandpass filtering. Large-amplitude surface waves and S waves were muted from the data, as they are not included in the acoustic-wave synthetic data.

5.2. Inversion of Synthetic Data

In order to test whether full-waveform inversion could detect the presence of a basement-like velocity discontinuity, full-waveform inversion was applied to synthetic data computed in the artificial model of Figure 11a. The synthetic data set was produced using the same shot and receiver geometry as the real data (e.g., Figure 3c). The starting model (Figure 11b) was derived from first arrival travel-time tomography, using travel-times calculated from the synthetic velocity model. As expected, travel-time tomography smoothed the sharp boundary shown by the black dash line so that it was not detected (Figure 11b).

The synthetic data were preprocessed in the same manner as would be used for the real data. The near offset data were muted to remove surface waves and very high amplitudes in the real data. The remaining data were windowed for 3 s after the first arrivals and band-pass filtered. The inversion was iteratively performed on a single frequency at a time, progressing gradually from 2 to 7 Hz (Table 1). The inversion for each higher frequency used the velocity model from the previous inversion as the starting model, stabilizing the inversion at shorter wavelengths. For each frequency, the source signature was inverted first from the most recent velocity model. Inversion for each frequency required eight iterations.

The velocity model after full-waveform inversion of 2–7 Hz data successfully sharpened the velocity contrast at the correct depth (Figure 11c). Although velocity oscillations common from waveform inversion were produced, the results resemble the true synthetic model and detect the discontinuity. The image quality is best at model distances of 8–14 km and 28–34 km, which are beneath the densest shots. This synthetic experiment shows that full waveform inversion can improve images of a discontinuity for the geometry of the SSIP experiment.

5.3. Inversion of SSIP Data

The same procedure and parameters (Table 1) were applied to the real SSIP data. The starting velocity model was the first-arrival travel-time tomography model from Figure 7 (Figure 12a). Short-offset data, bad seismic traces and a very noisy section of the data set was muted. The remaining data were windowed for 3 s after the first arrivals. The waveform-inversion result (Figure 12b) closely resembles the travel-time inversion velocity model, except for the high velocity below 2.5 km depth at distance 14–17 km. This part of the model is not as well constrained by the sparse shots above it, as suggested by the synthetic study, so is interpreted as an artifact. The model has short-wavelength oscillations about the starting model but shows no evidence for a sharp contrast that extends across the model (Figures 12 and 13). Waveform inversion confirms that the transition from sediment to crystalline rock velocity is gradual.

6. Metamorphism of Sediment

6.1. Seismic Evidence

The seismic velocity throughout the Imperial Valley increases continuously with depth from <2 km/s in surface sediment to >5 km/s (Figures 7−9 and 13−15) typical of crystalline rocks [e.g., *Christensen and Mooney*, 1995]. The high-quality seismic data are capable of detecting a sharp velocity contrast with depth, but such a discontinuity is not detected by a reflection arrival in the seismic data nor by full waveform inversion of the data. The mineralogy in geothermal energy and research boreholes indicates progressive metamorphism of Colorado River sediment with depth caused by the valley's high geothermal gradient [e.g., *Muffler and White*, 1969; *McDowell and Elders*, 1980; *Cho et al*., 1988; *Shearer et al*., 1988]. A previous seismic refraction study with several sparsely sampled lines also observed a lack of seismic bedrock reflector and a

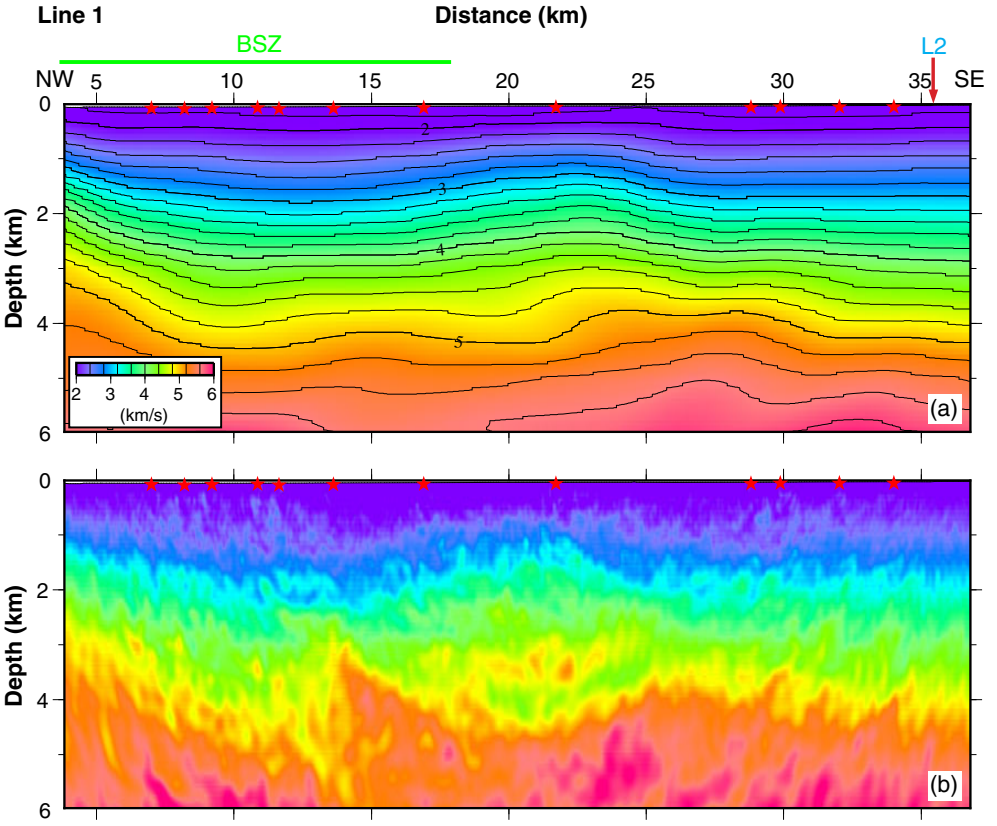

Figure 12. (a) Starting velocity model for full-waveform inversion from Figure 7. (b) Results of full-waveform inversion of the 2–7 Hz real data for the shots shown as stars. No sharp velocity discontinuity is produced.

low crystalline-rock velocity, and interpreted shallow crystalline rocks within the Imperial Valley to be metamorphosed sediment [*Fuis et al*., 1984]. The SSIP data provide higher-resolution seismic images that support and refine this interpretation.

Beyond the margins of the deep basin, the seismic data clearly show a much sharper velocity contrast from $<$3.5 to $\sim$6 km/s (e.g., west side of Figure 4). The starting velocity model, sparser shots, and smoothing used for the tomography do not ideally image the shallow sediment-rock transition outside the deep basin. However, the data are most consistent with 0–2 km of sediment deposited on pre-existing felsic crystalline bedrock with velocity near 6.0 km/s.

Throughout the Imperial Valley, the velocity gradient deeper than the $\sim$4.5 km/s contour is much smaller than that above $\sim$4.0 km/s (Figures 7$-$9 and 14 and 15). The velocity gradient at shallow depth varies within the valley from 0.8 up to 2 km/s/km, such that $\sim$4 km/s occurs at variable depth. This depth generally correlates with heat flow (Figures 2 and 16). At greater depth, the gradient is a much lower 0.4–0.5 s^{-1} almost down to the 6 km/s contour. The transition zone between high and low gradient is $\sim$1 km thick along line 1 and the central valley portions of lines 2 and 3. Toward the western margin of the deep basin along line 3 and both margins along line 2, the velocity gradient changes less sharply, but a strong change is still observed. The true change in gradient may be more gradational at these locations, or resolution might be worse because of the sparser shots and lateral smearing of the basin margins.

6.2. Correlation With Borehole Observations

The State 2-14 well of the Salton Sea Scientific Drilling Project [*Elders and Sass*, 1988] is located $<$0.5 km from seismic Line 3 (Figure 1), which enables correlation of the seismic velocity model with observations from the borehole (Figure 14). This research borehole penetrated 3.22 km of Pleistocene to Holocene sediment and metasedimentary rock in the Salton Sea geothermal field. Temperature in the borehole reached 300°C at 1700 m and 355°C at 3170 m (Figure 14e) [*Sass et al*., 1988]. Sedimentary layering and bulk

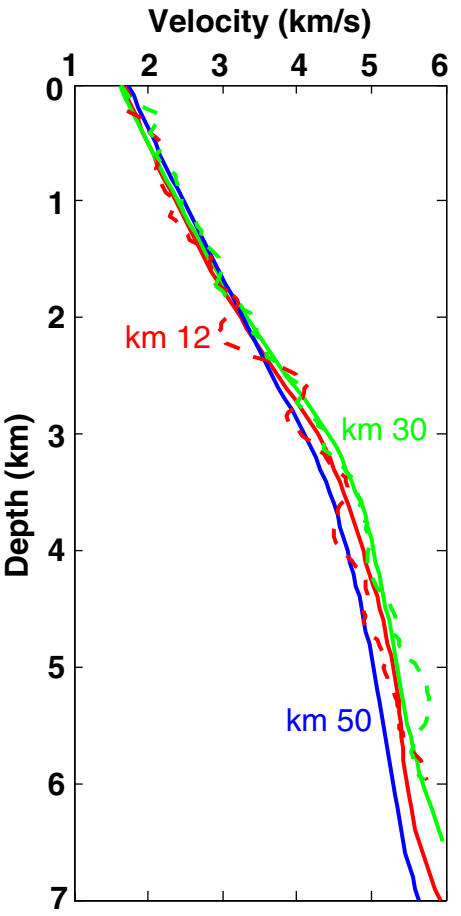

Figure 13. Velocity profiles at three locations along Line 1 at model km 12 (red), km 30 (green), and km 50 (blue). The solid lines are from first-arrival travel-time tomography (Figure 7), and the dashed lines from full-waveform inversion (Figure 12b). The velocity-depth profiles are averaged 500 m horizontally for travel-time tomography, and 200 m for full waveform inversion.

composition are preserved throughout the borehole and are consistent with a Colorado River source, but the sediment is progressively metamorphosed as temperature increases with depth [*Cho et al.*, 1988; *Shearer et al.*, 1988]. Three major metamorphic zones are observed from core samples (Figure 14a): chlorite-calcite (Chl-Cc) zone, biotite (Bt) zone, and clinopyroxene-amphibole (Cpx) zone. Epidote is formed beneath 0.9 km depth, at >250°C. The Chl-Cc zone beginning at 0.6 km depth and ~190°C represents greenschist facies metamorphism and the Cpx zone at ~3.0 km depth and ~350°C marks the low-pressure transition from greenschist to amphibolite facies [*Cho et al.*, 1988; *Shearer et al.*, 1988]. The rocks are progressively lithified in a manner similar to diagenesis, but without the formation of typical diagenetic minerals like zeolite. The metamorphism is driven primarily by the effects of temperature, except in sporadic steep fractures where hydrothermal fluids dominate. A regional 770 ka tuff is observed in the well at 1.7 km depth [*Herzig and Elders*, 1988; *Schmitt and Hulen*, 2008], indicating >2 km/Myr deposition and metamorphism of sediment that was deposited as recently as 300 kyr ago.

Seismic velocity measured in the borehole and from core samples [*Daley et al.*, 1988; *Paillet and Morin*, 1988; *Tarif et al.*, 1988] is consistent with the seismic velocity model from Line 3 (Figure 14b). The change in velocity gradient at 1.6–2.1 km depth occurs within the Chl-Cc metamorphic zone, and does not correlate with any metamorphic facies boundary or major mineral occurrence (Figure 14). It does, however, correlate with a change in gradient in the porosity (Figure 16d) and density of core samples [*Tarif et al.*, 1988] and in the electrical resistivity log [*Paillet and Morin*, 1988]. Most of the porosity is sedimentary matrix porosity, not fractures. Porosity decreases rapidly within the Chl-Cc zone from >20% to ~5% due to calcite precipitation, crystal overgrowth, and metamorphism of clays to feldspars and epidote [*Cho et al.*, 1988; *Tarif et al.*, 1988]. Once porosity reaches ~5%, metamorphism continues with depth, but porosity closes much more slowly, perhaps due to lower permeability and less fluid flow. The top of the change in gradient in seismic velocity is interpreted to be due to the change in gradient in porosity and density, not to the minerals present. This change occurs at a velocity of ~4.4 km/s, which is typical of a well-cemented, low-porosity shale or sandstone [e.g., *Han et al.*, 1986; *Eberhart-Phillips et al.*, 1989; *Johnston and Christensen*, 1995; *Vernik and Liu*, 1997]. This ~5% porosity is very high and seismic velocity is very low for a greenschist facies metasedimentary rock, probably due to the shallow depth and rapid speed of metamorphism. Consolidated, higher porosity, weaker metasedimentary rock starts at shallower depth, near the top of the Chl-Cc zone.

The same metamorphic mineralogy is observed in geothermal wells throughout the Imperial Valley [e.g., *Muffler and White*, 1969; *McDowell and Elders*, 1980]. The metamorphic reactions are observed at different depths due to different heat flow, but at very similar temperatures. The Elmore 1 well within the geothermal field near line 3 has much higher temperature (360°C at 2120 m depth), the metamorphic zones are shallower, and garnet is created near the bottom of the well [*McDowell and Elders*, 1980]. A change in porosity gradient at porosity ~9%, very similar to the State 2-14 well, occurs at ~1.3 km depth in the Elmore 1 well, but in middle of the Bt zone rather than the Chl-Cc zone.

Metamorphic mineralogy is available for few wells outside the geothermal field, where the heat flow is much lower but still much higher than normal continental values. The deep Wilson No. 1 well at the

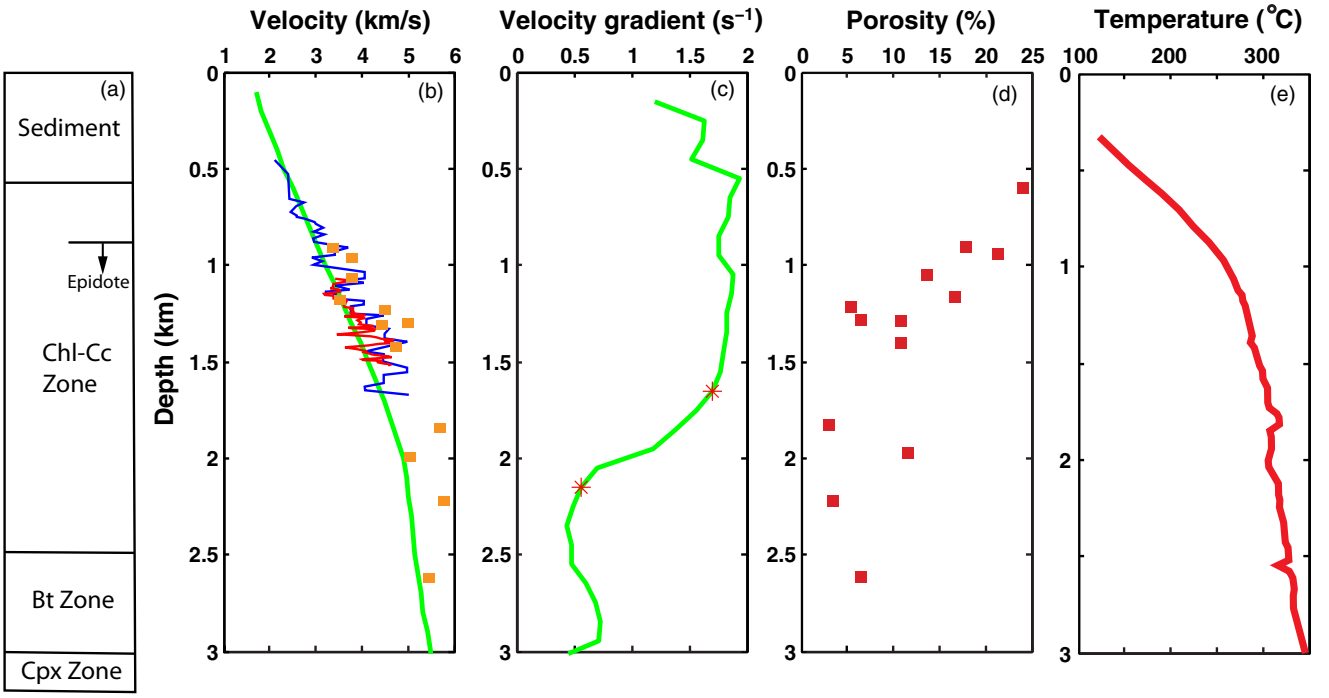

Figure 14. Correlation of the seismic velocity model with borehole observations from the State 2–14 well in the Salton Sea geothermal field. (a) Metamorphic zones from *Cho et al.* [1988]. (b) P-wave seismic velocity from this study (green), vertical seismic profiling in the well (blue) from *Daley et al.* [1988], sonic waveform log (red) from *Paillet and Morin* [1988], and ultrasonic measurements of core samples (orange) from *Tarif et al.* [1988]. (c) Velocity gradient from this study. (top and bottom) The transition zone in velocity gradient is marked by red stars. (d) Porosity of core samples from *Tarif et al.* [1988]. (e) Borehole temperature from *Sass et al.* [1988].

intersection of Lines 1 and 2, with a temperature typical of most of the valley (~260°C at 4.1 km depth), observed the same metamorphic reactions at similar temperatures but greater depth (Figure 15) [*Muffler and White*, 1969]. Due to lower temperature, epidote and the biotite zone were not observed. Porosity was

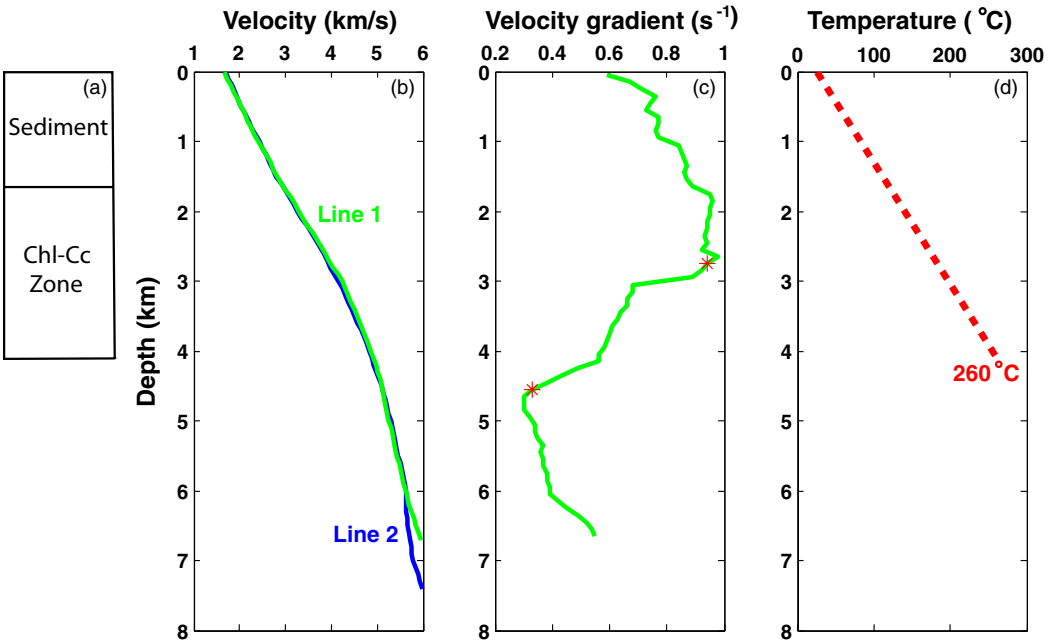

Figure 15. Correlation of seismic velocity profiles at the intersection of Lines 1 and 2 with the Wilson No. 1 well. (a) Metamorphic facies from *Muffler and White* [1969]. (b) Seismic velocity from Lines 1 (green) and 2 (blue) are consistent. (c) Velocity gradient from Figure 15b. The velocity gradient is very different above and below a transition zone (stars). (d) Well bottom temperature from *Muffler and White* [1969] projected linearly to the surface.

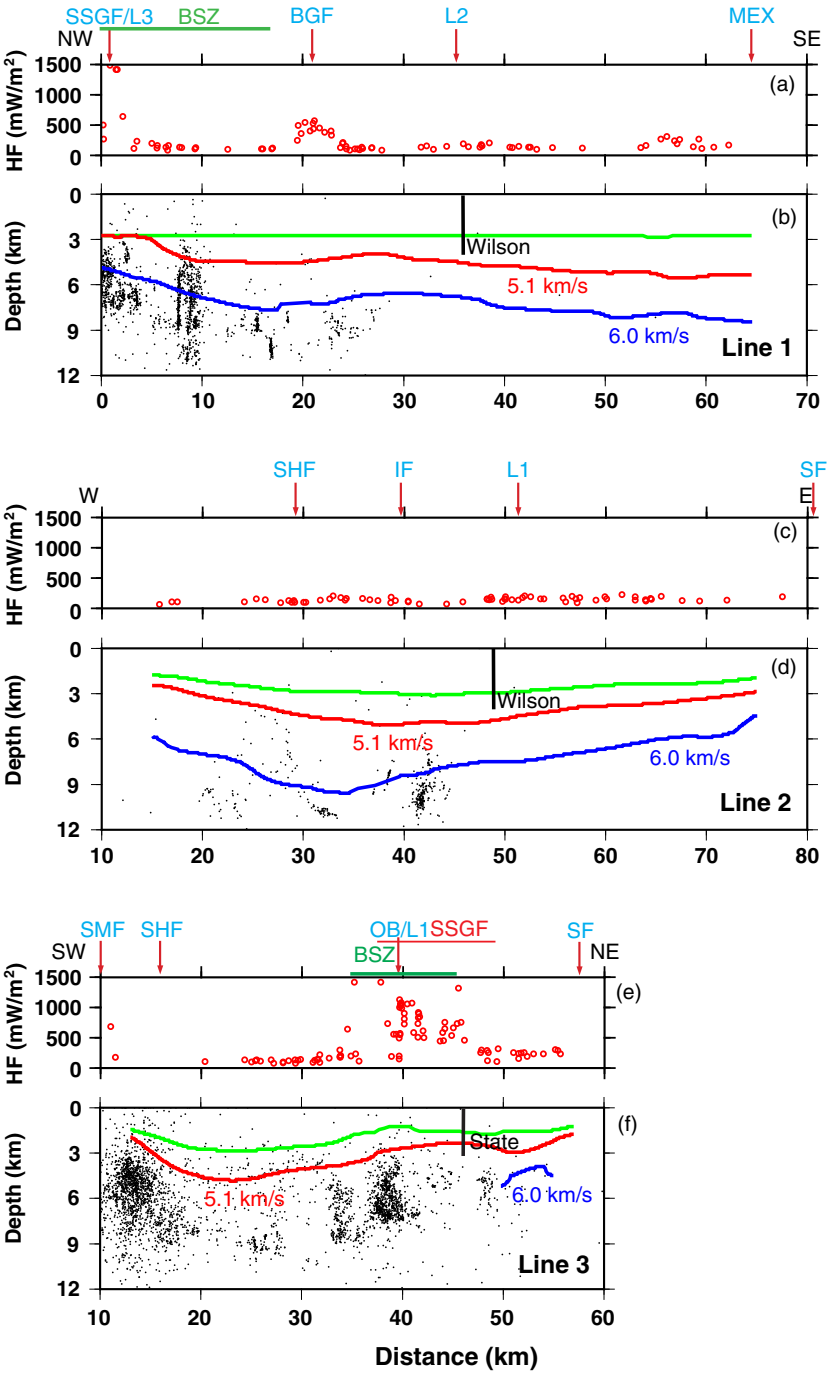

Figure 16. Interpretation of the seismic velocity models of Figures 7–9. For each seismic line, (top) heat flow from wells within 2 km of the seismic line (Figure 2). (bottom) Depth to features of the seismic velocity models. Green lines show the top of the change in velocity gradient. Within the Imperial Valley, this represents a greenschist-facies metasedimentary rock with 5–10% porosity. Red lines correspond to metasedimentary rocks with seismic velocity of 5.1 km/s. Blue lines correspond to the 6.0 km/s seismic velocity of preexisting crust outside the valley, which may not exist beneath the valley. Line 3 does not image deep enough to observe 6 km/s in the valley. *These lines do not represent boundaries, but are gradational changes due to progressive metamorphism. Metasediment continues to at least 7–8 km depth*. Black dots are seismicity within 5 km of the seismic line from *Hauksson et al*. [2012]. Geologic labels and wells are as for Figures 7–9.

mostly closed at an unreported depth within the Chl-Cc zone. Seismic velocity at this location is lower than in the geothermal field, and the change in velocity gradient occurs almost twice as deep at ~2.8 km depth, where the velocity is a very similar 4.0 km/s (Figure 15). This depth is within the Chl-Cc zone, but at lower metamorphic facies within the zone. The change in velocity gradient is interpreted to be due to a change in

porosity gradient at 5–10% porosity similar to that observed in the geothermal fields. Rapid closure of porosity always occurs within the Chl-Cc zone, indicating that metamorphism plays a role. However, at greater depth, it occurs at a lower temperature within the Chl-Cc zone. This suggests that while pressure plays only a minor role in the metamorphic mineralogy, metamorphism, and pressure work together to close porosity.

6.3. Depth and Extent of Metasedimentary Crust

The top of the sharp decrease in seismic velocity gradient is interpreted to be the depth where rapid closure of porosity ends, at 5–10% porosity. This depth was measured along all of the seismic lines (Figure 16). Even though the depth changes along the lines, it occurs at a fairly consistent velocity of ~4.1 km/s. In the geothermal fields, the velocity at this depth is up to 5% faster, representing a more intense metamorphism. Where the change in velocity gradient is not as sharply defined, 4.1 km/s was used as a proxy. At this depth (Figure 16), we interpret a greenschist-facies metasedimentary rock with 5–10% porosity due to rapid metamorphism at shallow depth. This "boundary" is in fact gradational due to progressive metamorphism with depth. It represents a change in the gradient of the closure of porosity rather than a metamorphic facies boundary. Metasedimentary rock with higher porosity exists well above this boundary, but the top of metamorphism and consolidation are not well expressed by geophysical parameters. The shallowest depth for this velocity-gradient boundary is 1.2–1.6 km in the Salton Sea geothermal field along Line 3 and at the northern end of Line 1 (Figure 16), where the heat flow exceeds 600 mW/m^2 [*Helgeson*, 1968; *Newmark et al*., 1988]. Most of the rest of the valley, however, has a much lower heat flow of 100–200 mW/m^2 (Figures 2 and 16) [*Lachenbruch et al*., 1985]. For the rest of the valley, the depth of the velocity-gradient boundary is at 2.5–3 km depth, and it is very flat at ~2.8 km depth along the axis of the valley on Line 1 (Figure 16). Little contrast is observed across the Imperial Fault, even though this transform fault bounds two different rift segments. The deepest boundary is along the western portion of Line 3, which extends west of the northwest extrapolation of the Imperial fault. This area lies outside the main rift. The velocity-gradient boundary is difficult to define near the margins of the valley due to sparser shots, shallower ray coverage, and lateral smoothing of the tomography model. It may not turn shallower toward the southwest as shown in Figure 16, except outside the basin.

At the eastern and western margins of the valley along Lines 2 and 3, the raw seismic data (e.g., Figure 4) indicate thinner sediment, a sharper sediment-rock boundary, and faster crystalline-rock velocity of ~6 km/s immediately beneath the sediment. These observations are interpreted as evidence for sediment deposition on preexisting crystalline crust outside the main rift valley. The margins of the deep basin are smeared by tomographic smoothing and sparser shots, but are still consistent with steep faults. Along Line 2, a change in slope of the velocity contours suggests a discontinuity at km ~30 (Figure 8), near the Superstition Hills Fault. The western boundary along Line 3 lies east of the Superstition Mountains, which expose granitic basement, and may be as far east as the Superstition Hills Fault (Figure 9). The eastern boundary of the basin is similar along lines 2 and 3 and is consistent with the Sand Hills Fault, which is thought to represent an inactive strike-slip fault that predates the modern active faults.

Metasedimentary crust extends to at least 7–8 km depth based on smoothly increasing seismic velocity that is slower than that observed outside the basin. Based on deposition rates of 2–4 km/Myr [*Schmitt and Hulen*, 2008], 8–16 km of sediment has been deposited in the last 4 Myr. Based on longer-offset SSIP data [*Han et al*., 2016], felsic crystalline rock extends to ~13 km depth. The entire felsic component of the crystalline crust may be metamorphosed synrift sediment. Alternatively, the lower ~5 km has seismic velocity that is also consistent with prerift granitic continental crust. *Dorsey* [2010] and *Dorsey and Lazear* [2013] show that the volume of sediment produced by erosion of the Colorado Plateau and carried to the Salton Trough by the Colorado River is consistent with the 8–13 km of sediment plus metasediment constrained by the seismic data.

Abundant seismicity occurs at 3–8 km depth in the Salton Sea geothermal field, 3–11 km depth in most of the Brawley Seismic Zone, and 8–11 km depth beneath the Imperial fault (Figure 16) [*Lin et al*., 2007; *Hauksson et al*., 2012]. A seismic velocity of 5.1 km/s is used as a rough proxy for stronger crystalline rock that might support seismic stress (Figure 16). In general, the shape of this velocity contour mimics the shallower velocity-gradient boundary at almost twice the depth. Most seismicity occurs deeper than this proxy. Within the Brawley Seismic Zone, abundant seismicity occurs at depths much shallower than 9 km, including events with magnitude ~5 [e.g., *Hauksson et al*., 2013]. Thus metamorphism is creating new crystalline crust that is strong enough for large-magnitude seismic brittle fracture. Imperial Fault seismicity occurs at depths that may correspond to prerift crust or higher-grade metasediment.

The interpreted metasedimentary rock is 5–10 km thick, from <3 to 8–13 km depth, which constitutes a significant fraction of the Imperial Valley crust that is only ~18 km thick [*Han et al*., 2016]. Assuming that continental rifting proceeds to seafloor spreading and an ocean basin, metamorphosed rift sediment will form a significant component of the passive continental margin. Based solely on geophysical properties, metamorphosed synrift sediment may be mistaken for extended preexisting continent. Since high heat flow and river deltas are expected during the late stages of continental breakup, metasediment may be an important and underrecognized component of global passive continental margins.

7. Conclusions

Three P-wave seismic velocity models in the Imperial Valley were generated from first arrival travel time tomography of the SSIP refraction data. The results are consistent with the previous study of *Fuis et al*. [1984], but provide more details on the basin structure and underlying crystalline rock. Velocity increases continuously with depth within the valley with no velocity discontinuity, indicating a gradational transition between sediment and underlying crystalline rock. This interpretation is confirmed by full waveform inversion on one of the seismic lines. Comparison with boreholes indicates that sediment within the basin is progressively metamorphosed at shallow depth by the high heat flow in the rift. This temperature-driven metamorphism continues with depth, producing strong, new crystalline rock. A regional sharp change in the seismic velocity gradient correlates to a change in the rate of closing porosity in wells. This change occurs within the greenschist facies, but at a porosity of 5–10% that is much higher than traditional metamorphism. This change in porosity gradient occurs at 2.5–3 km depth in most of the valley, but is much shallower at ~1.5 km depth in the Salton Sea geothermal field, corresponding to extremely high heat flow. Velocity more typical of strong crystalline rock is observed at almost twice these depths. Abundant seismicity within the Brawley seismic zone occurs within metamorphosed synrift sediment. Sedimentation and high heat flow are actively creating new crystalline crust in the Imperial Valley, and that crust is strong enough for brittle seismicity related to ongoing extension. This new, felsic crystalline crust will become a significant component of the future passive continental margin.

Acknowledgments

We thank the Editor Thorsten Becker and three anonymous reviewers for their helpful and constructive reviews. This research was supported by NSF MARGINS and EarthScope grants 0742263 to J.A.H. and 0742253 to J.M.S., by the U. S. Geological Survey's Multihazards Research Program, and by the Southern California Earthquake Center (SCEC) (Contribution No. 6244). We thank the >90 field volunteers and USGS personnel who made data acquisition possible. Numerous landowners acknowledged in *Rose et al*. [2013] allowed access for shots and stations. Seismographs and technical support were provided by the IRIS-PASSCAL instrument facility; special thanks go to Mouse Reusch and Patrick Bastien from PASSCAL for their field and data efforts. Software support was provided by Landmark Software and Services, a Halliburton Company. The data have been archived at the IRIS DMC (http://ds.iris.edu/pic-ph5/metadata/SSIP/form.php).

References

Bleibinhaus, F., R. W. Lester, and J. A. Hole (2009), Applying waveform inversion to wide-angle seismic surveys, *Tectonophysics*, *472*, 238–248, doi:10.1016/j.tecto.2008.08.023.

Brenders, A. J., and R. G. Pratt (2007a), Full waveform tomography for lithospheric imaging: Results from a blind test in a realistic crustal model, *Geophys. J. Int.*, *168*, 133–151, doi:10.1111/j.1365-246X.2006.03156.x.

Brenders, A. J., and R. G. Pratt (2007b), Efficient waveform tomography for lithospheric imaging: Implications for realistic, two-dimensional acquisition geometries and low-frequency data, *Geophys. J. Int.*, *169*, 152–170, doi:10.1111/j.1365-246X.2006.03096.x.

Cho, M., J. G. Liou, and D. K. Bird (1988), Prograde phase relations in the State 2-14 well metasandstones, Salton Sea geothermal field, California, *J. Geophys. Res.*, *93*, 13,081–13,103, doi:10.1029/JB093iB11p13081.

Christensen, N. I., and W. D. Mooney (1995), Seismic velocity structure and composition of the continental crust: A global view, *J. Geophys. Res.*, *100*, 9761–9788, doi:10.1029/95JB00259.

Daley, T. M., T. V. McEvilly, and E. L. Majer (1988), Analysis of P and S wave vertical seismic profile data from the Salton Sea Scientific Drilling Project, *J. Geophys. Res.*, *93*, 13,025–13,036, doi:10.1029/JB093iB11p13025.

Dorsey, R. J. (2010), Sedimentation and crustal recycling along an active oblique rift margin Salton Trough and northern Gulf of California, *Geology*, *38*, 443–446, doi:10.1130/G30698.1.

Dorsey, R. J., and G. Lazear (2013), A post-6 Ma sediment budget for the Colorado River, *Geosphere*, *9*, 781–791, doi:10.1130/GES00784.1.

Eberhart-Phillips, D., D. Han, and M. D. Zoback (1989), Empirical relationships among seismic velocity, effective pressure, porosity, and clay content in sandstone, *Geophysics*, *54*, 82–89, doi:10.1190/1.1442580.

Elders, W. A., and J. H. Sass (1988), The Salton Sea scientific drilling project, *J. Geophys. Res.*, *93*, 12,953–12,968, doi:10.1029/JB093iB11p12953.

Elders, W. A., R. W. Rex, T. Meidav, P. T. Robinson, and S. Bieler (1972), Crustal spreading in southern California, *Science*, *178*, 15–24, doi:10.1126/science.178.4056.15.

Fuis, G. S., and W. M. Mooney, J. H. Healy, G. A. McMechan, and W. J. Lutter (1984), A seismic refraction survey of the Imperial Valley region, California, *J. Geophys. Res.*, *89*, 1165–1189, doi:10.1029/JB089iB02p01165.

Han, D., A. Nur, and D. Morgan (1986), Effects of porosity and clay content on wave velocities in sandstones, *Geophysics*, *51*, 2093–2107, doi:10.1190/1.1442062.

Han, L., et al. (2016), Continental rupture and the creation of new crust in the Salton Trough rift, southern California and northern Mexico: Results from the Salton Seismic Imaging Project, *J. Geophys. Res. Solid Earth*, *121*, doi:10.1002/2016JB013139.

Hauksson, E., W. Yang, and P. M. Shearer (2012), Waveform relocated earthquake catalog for Southern California (1981 to June 2011), *Bull. Seismol. Soc. Am.*, *102*, 2239–2244. doi:10.1785/0120120010.

Hauksson, E., et al. (2013), Report on the August 2012 Brawley earthquake swarm in Imperial Valley, Southern California, *Seismol. Res. Lett.*, *84*(2), 177–189, doi:10.1785/0220120169.

Helgeson, H. C. (1968), Geologic and thermodynamic characteristics of the Salton Sea geothermal system, *Am. J. Sci.*, *266*, 129–166, doi:10.2475/ajs.266.3.129.

Herzig, C. T., and W. A. Elders (1988), Nature and significance of igneous rocks cored in the State 2-14 research borehole: Salton Sea Scientific Drilling Project, California, *J. Geophys. Res.*, *93*, 13,069–13,080, doi:10.1029/JB093iB11p13069.
Herzig, C. T., J. M. Mehegan, and C. E. Stelting (1988), Lithostratigraphy of the State 2-14 borehole: Salton Sea Scientific Drilling Project, *J. Geophys. Res.*, *93*, 12,969–12,980, doi:10.1029/JB093iB11p12969.
Hole, J. A. (1992), Nonlinear high-resolution three-dimensional seismic travel time tomography, *J. Geophys. Res.*, *97*, 6553–6562, doi:10.1029/92JB00235.
Hole, J. A., and B. C. Zelt (1995), 3-D finite-difference reflection traveltimes, *Geophys. J. Int.*, *121*(2), 427–434, doi:10.1111/j.1365-246X.1995.tb05723.x.
Jennings, C. W., and W. A. Bryant (2010), Active Fault Map of California, Geologic Data Map No. 6, Scale 1:750,000, Calif. Geol. Surv., Sacramento.
Johnston, J. E., and N. I. Christensen (1995), Seismic anisotropy of shales, *J. Geophys. Res.*, *100*, 5991–6003, doi:10.1029/95JB00031.
Lachenbruch, A. H., J. H. Sass, and S. P. Galanis, Jr. (1985), Heat flow in southernmost California and the origin of the Salton Trough, *J. Geophys. Res.*, *90*, 6709–6736, doi:10.1029/JB090iB08p06709.
Larsen, S., and R. Reilinger (1991), Age constraints for the present fault configuration in the Imperial Valley, California: Evidence for northwestward propagation of the Gulf of California rift system, *J. Geophys. Res.*, *96*, 10,339–10,346, doi:10.1029/91JB00618.
Lin, G., P. M. Shearer, and E. Hauksson (2007), Applying a three-dimensional velocity model, waveform cross correlation, and cluster analysis to locate southern California seismicity from 1981 to 2005, *J. Geophys. Res.*, *112*, B12309, doi:10.1029/2007JB004986.
Lonsdale, P. (1989), Chapter 26: Geology and tectonic history of the Gulf of California, in *The Eastern Pacific Ocean and Hawaii, The Geological Society of America, The Geology of North America*, vol. N, edited by E. L. Winterer, D. M. Hussong, and R. W. Decker, pp. 499–521, *Geol. Soc. Am.*, Boulder, Colo.
Magistrale, H. (2002), The relation of the southern San Jacinto fault zone to the Imperial and Cerro Prieto faults, in A. Barth, ed., Contributions to crustal evolution of the southwestern United States, *Geol. Soc. Am. Spec. Pap.*, *365*, 271–278.
Magistrale, H., H. Kanamori, and C. Jones (1992), Forward and inverse three-dimensional P wave velocity models of the southern California crust, *J. Geophys. Res.*, *97*, 14,115–14,135, doi:10.1029/92JB00494.
Magistrale, H., S. Day, R. W. Clayton, and R. Graves (2000), The SCEC southern California reference three-dimensional seismic velocity model version 2, *Bull. Seismol. Soc. Am.*, *90*, S65–S76, doi:10.1785/0120000510.
McDowell, S. D., and W. A. Elders (1980), Authigenic layer silicate minerals in borehole Elmore 1, Salton Sea geothermal field, California, USA, *Contrib. Mineral. Petrol.*, *74*, 293–310, doi:10.1007/BF00371699.
McMechan, G. A., and W. D. Mooney (1980), Asymptotic ray theory and synthetic seismogram for laterally varying structures: Theory and application to the Imperial Valley, California, *Bull. Seismol. Soc. Am.*, *70*, 2021–2035.
Muffler, L. J. P., and B. R. Doe (1968), Composition and mean age of detritus of the Colorado River delta in the Salton Trough, southeastern California, *J. Sediment. Petrol.*, *38*, 384–399.
Muffler, L. J. P., and D. E. White (1969), Active metamorphism of upper Cenozoic sediments in the Salton Sea geothermal field and the Salton Trough, southeastern California, *Geol. Soc. Am. Bull.*, *80*, 157–182, doi:10.1130/0016-7606(1969)80[157:AMOUCS]2.0.CO;2.
Newmark, R. L., P. W. Kasameyer, and L. W. Younker (1988), Shallow drilling in the Salton Sea region: The thermal anomaly, *J. Geophys. Res.*, *93*, 13,005–13,023, doi:10.1029/JB093iB11p13005.
Paillet, F. L., and R. H. Morin (1988), Analysis of geophysical well logs obtained in the State 2-14 borehole, Salton Sea geothermal area, California, *J. Geophys. Res.*, *93*, 12,981–12,994, doi:10.1029/JB093iB11p12981.
Persaud, P., Y. Ma, J. M. Stock, J. A. Hole, G. S. Fuis, and L. Han (2016), Fault zone characteristics and basin complexity in the southern Salton Trough, California, *Geology*, *44*(9), 747–750, doi:10.1130/G38033.1.
Pratt, P. G. (1999), Seismic waveform inversion in the frequency domain, part 1: Theory and verification in a physical scale model, *Geophysics*, *64*, 888–901, doi:10.1190/1.1444597.
Robinson, P. T., W. A. Elders, and L. J. P. Muffler (1976), Quaternary volcanism in the Salton Sea geothermal field, Imperial Valley, California, *Geol. Soc. Am. Bull.*, *87*, 347–360, doi:10.1130/0016-7606(1976)87 < 347:QVITSS>2.0.CO;2.
Rose, E. J., et al. (2013), Borehole-explosion and air-gun data acquired in the 2011 Salton Seismic Imaging Project (SSIP), southern California-Description of the survey, *U.S. Geol. Surv. Open File Rep.*, 2013-1172, 84 p., doi:10.3133/ofr20131172.
Sass, J. H., S. S. Priest, L. E. Duda, C. C. Carson, J. D. Hendricks, and L. C. Robison (1988), Thermal regime of the State 2-14 well, Salton Sea Scientific Drilling Project, *J. Geophys. Res.*, *93*, 12,995–13,004, doi:10.1029/JB093iB11p12995.
Schmitt, A. K., and J. B. Hulen (2008), Buried rhyolites within the active, high-temperature Salton Sea geothermal system, *J. Volcanol. Geotherm. Res.*, *178*(4), 708–718, doi:10.1016/j.jvolgeores.2008.09.001.
Schmitt, A. K., and J. A. Vazquez (2006), Alteration and remelting of nascent oceanic crust during continental rupture: Evidence from zircon geochemistry of rhyolites and xenoliths from the Salton Trough, California, *Earth Planet. Sci. Lett.*, *252*, 260–274, doi:10.1016/j.epsl.2006.09.041.
Shearer, C. K., J. J. Papike, S. B. Simon, and B. L. Davis (1988), Mineral reactions in altered sediments from the California state 2-14 well: Variations in the model mineralogy, mineral chemistry and bulk composition of the Salton Sea scientific drilling project core, *J. Geophys. Res.*, *93*, 13,104–13,122, doi:10.1029/JB093iB11p13104.
Smithyman, B. R., and R. M. Clowes (2012), Waveform tomography of field vibroseis data using an approximate 2D geometry leads to improved velocity models, *Geophysics*, *77*, R33–R43, doi:10.1190/GEO2011-0076.1.
Stock, J. M., and K. V. Hodges (1989), Pre-Pliocene extension around the gulf of California and the transfer of Baja California to the pacific plate, *Tectonics*, *8*, 99–115, doi:10.1029/TC008i001p00099.
Tarif, P. A., R. H. Wilkens, C. H. Cheng, and F. L. Paillet (1988), Laboratory studies of the acoustic properties of samples from Salton Sea Scientific Drilling Project and their relation to microstructure and field measurements, *J. Geophys. Res.*, *93*, 13,057–13,067.
Vernik, L., and X. Liu (1997), Velocity anisotropy in shales: A petrophysical study, *Geophysics*, *62*, 521–532, doi:10.1190/1.1444162.